Title	Topological optimization for tailored designs of advection-diffusion-reaction porous reactors based on pore scale modeling and simulation: A PNM-NSGA framework
Author(s)	Alizadeh, Mehrzad; Gostick, Jeff; Suzuki, Takahiro et al.
Citation	Computers & Structures. 2024, 301, p. 107452
Version Type	VoR
URL	https://hdl.handle.net/11094/96457
rights	This article is licensed under a Creative Commons Attribution-NonCommercial 4.0 International License.
Note	

Computers and Structures 301 (2024) 107452

Contents lists available at ScienceDirect

Computers and Structures

journal homepage: www.elsevier.com/locate/compstruc

Topological optimization for tailored designs of advection–diffusion-reaction porous reactors based on pore scale modeling and simulation: A PNM-NSGA framework

Mehrzad Alizadeh [a,*], Jeff Gostick [a,b], Takahiro Suzuki [a], Shohji Tsushima [a]

[a] Department of Mechanical Engineering, Graduate School of Engineering, Osaka University, Suita, Osaka 5665-0871, Japan
[b] Department of Chemical Engineering, University of Waterloo, Waterloo, Ontario N2L 3G1, Canada

ARTICLE INFO

Keywords:
Pore network modeling
Optimization
Genetic algorithm
Advection-diffusion–reaction
Porous reactor

ABSTRACT

Reactive transport within porous reactors is crucial to many diverse applications, and the efficacy of these reactors hinges on their microstructure. Mathematical modeling and optimization play a pivotal role in the exploration of efficient designs, enabling the generation of structures that may not be achievable through random realizations of packings. In this study, we propose a framework for high-resolution topological optimization of porous flow-through reactors based on pore-scale simulations using a non-dominated sorting genetic algorithm II. A pore network model for an advection–diffusion-reaction system is developed to simulate reactor performance. This model is integrated with a mathematical optimization algorithm, incorporating a background grid and Delaunay tessellation. The optimization framework generates enhanced porous structures, simultaneously maximizing conversion rates while minimizing pumping costs. Striking a balance between permeability and reactive surface area, the final designs yield a set of Pareto optimal solutions, encompassing diverse non-dominated designs with varying reaction rates and hydraulic requirements. The results demonstrate that optimal pore configurations lead to a 280% increase in conversion rates and a 6% reduction in pumping costs at one end, while on the opposite end of the Pareto front, a 15.2% increase in reaction rates and an 11.3% reduction in pumping costs are observed.

1. Introduction

Porous reactors are found in a variety of applications, including redox batteries, fuel cells, and catalytic reactors [1–3]. The reactive transport occurring within these porous media includes advection and diffusion of reactive species in single- or multi-phase fluids, as well as singular or multiple (electro-) chemical reactions. The porous matrix provides the active surface area on which heterogeneous catalytic reactions occur and also facilitates the flow of heat and charge. The void space provides pathways for the flow of reactive and product species, and carrier fluids. Consequently, reactor performance, hydraulic efficiency, operational costs, and durability of porous reactors are intertwined with the microstructural characteristics. For instance, achieving a higher reaction rate can be accomplished by increasing the surface area, which is most readily achieved by incorporation of smaller pores, but this generally hinders flow and diffusion of reactant. Hence, optimizing overall performance entails balancing between maximizing surface area and minimizing mass transport resistance. An ideal porous reactor should consist of pores of varying size and appropriate distribution to enhance both surface area and mass transfer concurrently. Recent progress in additive manufacturing and 3D printing technologies has unlocked fresh prospects for the fabrication of porous reactors featuring complex microarchitectures, offering promising advances in fields such as catalysis [4], electrochemistry [5,6], and pharmaceuticals [7]. However, leveraging the full potential of these fabrication methods requires a finely tuned design of the porous microstructure. Several experimental investigations have explored tailored reactors with engineered structures to enhance performance [8–10]. For instance, Xu et al. [8] proposed an electrospinning method to fabricate a free-standing carbon nano-fibrous web with ultra-large pores for vanadium redox flow batteries (VRFBs). Their findings showed that the new design reduces concentration polarization, resulting in a VRFB with 10.3% higher voltage efficiency and double the electrolyte utilization efficiency compared to traditional electrodes at a current density of $60 \mathrm{mA\,cm^{-2}}$. Despite these promising results, performing comprehensive parametric

---

[*] Corresponding author.
E-mail address: alizadeh.mehrzad@gmail.com (M. Alizadeh).

https://doi.org/10.1016/j.compstruc.2024.107452
Received 19 March 2024; Accepted 8 June 2024

Nomenclature

A_s	Wetted surface area (m^2)
C	Concentration $(mol\,m^{-3})$
d	Voxel (spacing) size (m)
D_A	Solute diffusion coefficient (m^2s^{-1})
D_t	Throat diameter (m)
F_{obj}	Objective function
G	Total conductance $(m^3s^{-1}Pa^{-1}$ or $m^2s^{-1})$
g	Conductance $(m^3s^{-1}Pa^{-1}$ or $m^2s^{-1})$
k_L	Mass transfer coefficient (ms^{-1})
k_r	Reaction constant (ms^{-1})
L_p	Pore segment length (m)
L_t	Throat length (m)
n_g	Number of genomes (candidate pores)
n_{pop}	Population size
p_c	Crossover ratio
p_m	Mutation ratio
Pe	Peclet number
Q	Volumetric flow rate (m^3s^{-1})
r	Radius (m)
r_A	Reaction rate $(mol\,s^{-1})$
r_m	Mutation rate
p	Pressure (Pa)
Greek symbols	
μ	Viscosity (Pa s)
ρ	Density $(kg\,m^{-3})$
Subscripts/superscripts	
d	Diffusive
h	Hydraulic
p	Pore
$surf$	Surface
t	Throat

studies to pinpoint the optimal structural parameters (e.g., pore size) remains challenging due to the cost and time associated with experiments. Evidently, achieving a fully optimal topology (including factors like the ideal pore size and spatial distribution) through experimental trial and error appears to be a daunting task. Alternatively, mathematical modeling and optimization offer a systematic approach to investigate the structure-performance relationship and generate more efficient designs [11–16]. For instance, topology optimization using continuum macroscale models has been successfully utilized for optimizing reactive transport in porous media. In a recent study by Roy et al.[17], researchers employed a density-based topology optimization method to automatically optimize the distribution of porosity throughout the electrode of VRFBs. Their optimized designs reduced losses caused by overpotentials by up to 84%. Additionally, Mitchell and Ortiz [18] employed density-based topology optimization to enhance the anode electrode structure of a lithium-ion battery. By improving the sluggish electron transport caused by the low intrinsic electrical conductivity of silicon, they significantly enhanced the electrode performance. While these approaches provide a powerful tool for optimizing macroscopic material properties (e.g., porosity), they are typically unable to optimize the porous microstructure at the pore level. Particularly, since the interactions between the aforementioned transport and rate processes happen at a pore level, a pore-scale mathematical model becomes imperative for precise simulation of reactor behavior under varying structural and operational conditions. Moreover, in advection–diffusion–reaction (ADR) systems, around which this study revolves, several conflicting objectives must be met simultaneously, namely high conversion rate, low mass transport resistance, and low pumping cost. The absence of trade-offs among these objectives gives rise to a multi-objective optimization (MOO) problem, wherein a set of Pareto optimal (nondominated) solutions can be attained. Another emerging trend is the utilization of particle-scale models, such as the lattice Boltzmann method (LBM), together with topology optimization algorithms. In a paper published in 2024, Zheng et al.[19] utilized LBM coupled with level-set topology optimization to generate optimized porous diffusion–reaction systems with hierarchical structures. Their optimization yielded structures with enhanced reaction rates and material utilization. However, their study only considers diffusion and reaction processes, without incorporating any convective flow. Currently, integration of LBM and topology optimization in the literature is limited and does not encompass various complicated transport and rate processes.

Mathematical models for reactive transport can be broadly classified into two primary categories: (1) macro-scale continuum models and (2) pore-scale models. In practical applications, porous reactors exhibit a diverse and heterogeneous structure. However, macro-scale continuum models assume uniform, averaged properties – such as flow resistance, thermal resistance, and reaction activity – within a representative elementary volume (REV). These models typically describe porous media using multiple isotropic and anisotropic properties (e.g. porosity, tortuosity, permeability coefficient). Although this approach offers valuable insights into reactive transport phenomena, it falls short in capturing the impact of the detailed microstructure at a high resolution – a necessity for precise simulation and design of porous reactors. In contrast, pore-scale models offer a geometrically resolved simulation of the system, addressing flow, transport, and reactions at a pore level. While this approach comes with increased computational requirements, it enables a thorough and dependable insight into the 3D morphology of porous reactors, resulting in a more robust comprehension of the structure-performance relationship. Numerous studies in the literature have introduced pore-scale models aimed at analyzing transport and rate processes within porous media across a range of applications [20–27]. For example, Zhan et al [21] employed a 3D pore-scale lattice Boltzmann method (LBM) to simulate transport mechanisms and electrochemical processes within VRFB electrodes. Their investigation revealed a critical link between the microstructure of the electrode and its electrochemical performance. They concluded that an optimal microstructure with a single dominant pore size peak (around 10 –20μm) and some large pores is essential for achieving both superior electrochemical performance and low-pressure drop, which are crucial for reducing operational costs. In another application, Kočí et al [22] introduced a novel methodology for pore-scale simulation of flow, diffusion, and reaction in coated catalytic filters. They accomplished this using 3D reconstructions of porous structures based on X-ray tomography (XRT). The reconstructed medium was then used for simulation in OpenFOAM using the finite volume method (FVM). Their results highlight that gas primarily flows through cracks in the coated layer and remaining free pores in the filter wall, with mass transport driven by diffusion. The results also underscored that compact catalytic coatings lead to a significant increase in pressure drop due to reduced local permeability.

While geometrically resolved models offer valuable insights into reactive transport phenomena, it is well-known that direct numerical simulation (DNS) demands substantial computational resources and is often limited to unreasonably small calculation domains [28]. Therefore, modeling an entire component (e.g., an electrode of a battery) or device (e.g., a battery cell) with a realistic length scale remains a challenge through these approaches. Also, the majority of these studies have concentrated on existing materials and structures [29], while pursuit of a systematic technique in generating novel optimal designs is not yet well studied. This is partly because mathematical optimization algorithms usually involve iterative model solutions, requiring extensive computational resources to seek even a single local optimum solution. In light of these constraints, it becomes evident that topological optimizing using geometrically resolved pore scale models is not yet feasible, at least with reasonable computational resources.

Pore network modeling (PNM)[30–32] represents an alternative approach to DNS, simplifying the intricate microstructure of porous media into a network of interconnected pores and straight tubes (throats). This abstraction accelerates simulations by several orders of magnitude (typically > 10000 times faster) compared to conventional pore-scale DNS models while maintaining an acceptable level of pore-scale accuracy. The computational efficiency of PNM positions it as a viable alternative for large-scale mathematical optimization of porous microstructures at a geometrically resolved level. PNM has been successfully employed to investigate various physical phenomena in different systems—diffusion in fuel cells [33], electrochemical reactive transport in battery electrodes [1], dispersion in porous media [34], and two-phase flow [35] to name a few. For example, in a recent publication, Misaghian et al [1] extended PNM to include multiple coupled physical processes to assess the influence of heterogeneous electrode structures on a VRFB cell performance, solving the advection–diffusion and Nernst-Planck equations for ion transport coupled with Butler-Volmer kinetics and solid–liquid mass transfer films. Their findings demonstrated that multi-layer structures with higher permeability near the membrane and lower permeability near the channel substantially increased current density, resulting in a remarkable 57% performance enhancement compared to the opposite layer arrangement.

Furthermore, Sadeghi et al [28] introduced a PNM-based framework to investigate reactive transport within hierarchical porous catalyst particles, emphasizing the generation of optimal microstructures rather than exclusively modeling existing porous media. Notably, the study finds that increasing macroporosity does not always enhance catalytic activity, and particles with lower pore size ratios exhibit higher reactivity. Subsequently, another research group extended this study into 3D [36], incorporating pore interconnections as an adjustable parameter. It has been found that particle performance exhibits distinct trends, influenced by macroporosity and other factors, depending on the average pore Damköhler number. Also of note is that the advantages of hierarchical structures are most pronounced in systems where the reaction-controlled process is absent, and species diffusivity is the limiting factor for reactive transport. Following these earlier research endeavors, Huang et al [30] investigates the influence of adding channels to a porous reactor with a first-order chemical reaction. After validating their PNM model against a finite element method (FEM), they showed that the addition of channels in these structures significantly enhances mass transport, making multi-channel featured porous systems desirable for catalyst applications. Nevertheless, although these studies yielded valuable results, their proposed frameworks lack a comprehensive mathematical scheme for generating innovative microstructures automatically. Instead, they often presuppose certain characteristics of the optimal microstructure, such as the presence of macroporosity or extended channels, primarily conducting parametric analysis on various parameters. In a more rigorous approach, van Gorp et al [29] integrated a genetic algorithm (GA) with PNM to design highly efficient electrodes for VRFBs. Their optimized design effectively reduced pumping costs by 73% and improved electrochemical performance by 42% compared to a randomly generated initial structure. Although that study provided a valuable proof-of-concept, it was limited in several regards. The pores were confined to a cubic lattice with a relatively limited number of pores (a total of 676 pores), which also limited the size distribution that could be attained. Their model did not account for the influence of local convective flow (local Reynolds number) when estimating the mass transfer coefficient for the transport of species from the bulk solution to the solid–liquid interface. Instead, a uniform Reynolds number was assumed throughout the domain, based on the superficial velocity. Additionally, they manually maintained overall porosity at a constant value during the optimization process. As such, their framework did not encompass the capacity to generate entirely distinct pore network (PN) topologies.

The primary objective of this study is to present a framework for the large-scale optimization of porous reactors by integrating PNM and a non-dominated sorting genetic algorithm II (NSGA-II). This framework specifically addresses advection, diffusion, and chemical reaction phenomena within a porous network, which is generated using a Delaunay tessellation of random base points [37]. By employing a Delaunay tessellation, the optimization algorithm gained the flexibility to distribute pores in arbitrary spatial configurations, in contrast to previous efforts which were limited to a cubic lattice. The network generation and simulations are conducted using OpenPNM, a Python-based open-source package developed for PN simulations [38]. Moreover, the optimization process is carried out through NSGA-II, allowing for theres simultaneous optimization of multiple objectives. In this study, the focus is on two key objectives: conversion rate and pumping cost. However, it is worth noting that this framework is versatile and capable of accommodating any number of objectives as needed.

2. Modeling and optimization

In many practical applications, diverse and concurrent processes (e.g., advection, diffusion, and reaction) compete within porous reactors, collectively shaping their overall performance. Should any one of these processes impose limitations, it may degrade the overall performance. Given the significant influence of porous microstructure on these processes, the topology of porous networks should seek a balance among different processes without imposing severe limitations on any of them [39–41]. Furthermore, such systems frequently necessitate the simultaneous optimization of multiple conflicting objectives. For instance, in the context of ADR porous reactors, it is favorable to maximize the overall conversion rate while minimizing the hydraulic power requirements (pumping cost). Therefore, a MOO algorithm becomes a requisite tool to concurrently satisfy these diverse and contradictory requirements. In the present study, a designated set of points is provided as input for the network generation algorithm to create the PN. This constructed PN is subsequently used to solve flow and reaction in accordance with predetermined boundary conditions (BCs). The PNM simulation is in turn incorporated into an optimization algorithm, enabling the systematic refinement of the porous topology through an iterative process. Further details on these steps are provided in the following subsections.

2.1. Network generation

Transport through the PN depends not only on the pore size distribution, but also on the spatial and topological arrangement of the pores. Recent work by van Gorp et al [29] demonstrated the ability of genetic algorithm-based optimization to generate improve electrode performance by adjusting the pore size distribution and their spatial distribution on a cubic lattice. Confining the pore centers to a cubic lattice restricted the possible designs in several ways: the maximum pore size could not exceed the lattice spacing (lest pores overlap), the connectivity distribution was limited to 6 neighbors, and all connections between pores were oriented along the principal axis of the lattice. The present work aimed to overcome these limitations by developing a procedure for using random PNs based on Delaunay tessellations. Generating a PN from a Delaunay tessellation has been described in detail previously [37]. This procedure is outlined in subsection 2.1.1.

The communication between PNM and NSGA-II lies in the network generation process. On the PNM side, network generation is performed using a Delaunay tessellation in OpenPNM. It receives the coordinates of

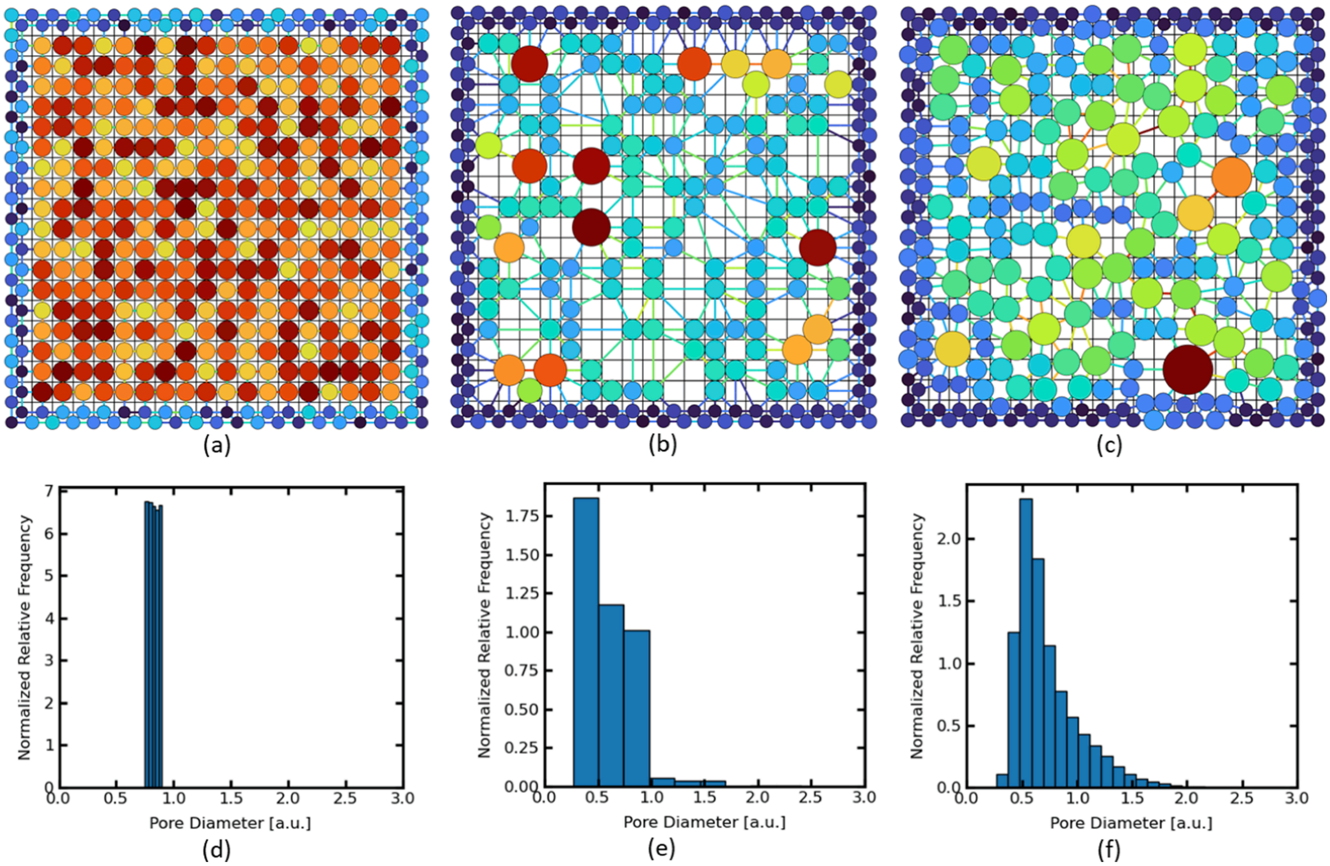

Fig. 1. 2D schematic of random network generation on a grid. The subfigures show results (a) when all possible locations are used, (b) with using only 30% of possible locations, and (c) using 30% *possible* location with relaxation of the base points. The bottom row shows the corresponding pore size distributions (in arbitrary units) attained by assuming all pore diameters are between 90 and 100% of the distance to their nearest neighbor.

some base points to generate a network. The background grid specifies the coordinates of all possible pores in the design domain. The optimizer, NSGA-II, tries to improve the structural design by selecting these possible coordinates from the background grid. It does this by including or excluding them in an algorithmic way, to enhance the objective functions (maximizing reaction rate and minimizing pumping requirements).

2.1.1. Generating random network topology

The main challenge when coupling random networks to genetic optimization is the incompatibility between having a fixed number of genes in each individual and each generation, and the infinite possible locations of pores. To address this, we defined a grid of *possible* locations and setup the genetic algorithm to optimize which of these locations were activated (described in section 2.4). The grid of possible location essentially adds a lower limit to the resolution of the pore locations. A resolution of 40μm was chosen meaning that the smallest pores size and smallest pore-to-pore space cannot be less than this if no other operator is applied. Fig. 1(a) shows the result of applying a Delaunay tessellation on a grid, which yields a standard cubic lattice, while Fig. 1(b) shows the result after randomly activating 30% of the sites on the grid. In this case the pore centers still lie on the grid, but the connectivity of the pores is more diverse than on a fixed lattice. The pore size distribution, shown in Fig. 1(e), is also wider than a cubic lattice (Fig. 1(e)) because the pore diameters were able to grow up the distance of the nearest pore rather than the fixed lattice spacing. The randomized network shown in Fig. 1 (b) was further enhanced by applying a relaxation of the pore centers after the tessellation. A rigorous relaxation as described by Lloyd [42] uses the geometric centroid of each Voronoi cell, which requires computing many convex hulls and is time consuming. An alternative, less computationally demanding, relaxation method was performed here such that new pore locations were computed as the distance-weighted average of each neighbor pore. This relaxation was applied iteratively by moving the pore centers halfway to the new locations to avoid overcorrecting, then repeated N times by recomputing the weighted average after each step. It was found that $N = 3$ provided a good balance between stable results and efficient computation. The final result is shown in Fig. 1(c) where it can be seen that most pore centers no longer lie on the grid and the distribution of the pores fills space. The pore size distribution in Fig. 1(f) is even broader than the case in Fig. 1(e). The sites along the edges and faces of the domain were always included to ensure that the internal pores were confined to a fixed domain size. The pores on the inlet and outlet faces were used to apply boundary conditions so did not affect the flow through the domain. The layer of small pores on the other surfaces can be considered as physically compacted or compressed so not relevant to the flow. All simulation results reported below were obtained on a 3D network, and the 2D representation shown in Fig. 1 is only to aid visualization.

2.1.2. Assigning geometric properties

Once the spatial locations of the pores and their connectivity was established, the geometric properties of the pores and throats were calculated. Pore radii were assigned by finding the maximum possible size of each pore that just touched its nearest neighbor, then multiplying this value by a random number between 0.75 and 0.9. Throat diameters were assigned by finding the minimum diameter of the two neighboring pores, then multiplying this value by a random number between 0.5 and 0.7 to create constrictions. The aforementioned ranges are chosen arbitrarily but they fall within the range of previously reported values in the literature [29,30]. Pores were treated as spheres and throats as

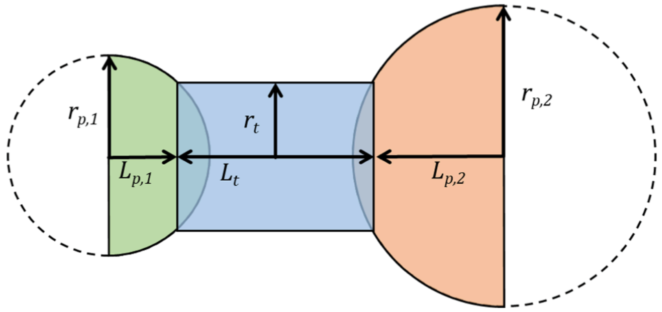

Fig. 2. Schematic diagram showing the assumed shape and pertinent dimensions for calculating transport conductance values.

cylinders for all subsequent geometry calculations such as surface areas and volumes. Throat lengths were computed by assigning the overlap between the spherical pore bodies and cylindrical throats to the throat. This is illustrated in Fig. 2.

2.1.3. *Adding throat nodes*

As will be discussed in section 2.2, it was necessary to incorporate local mass transfer coefficients in the reaction term. Mass transfer coefficients are a function of local fluid velocity, which is only known in the throats, while the reaction is also a function of concentration, which is only known in the pores. It was therefore necessary to incorporate throat nodes into the network, as described by Misaghian et al [1]. Each throat was divided into two segments and a new "node" (i.e., a pore) was inserted at the junction. The fluid velocity through this node could then be found from the upstream throat segment. The reaction term was only enabled in these throat nodes. This process increased the number of degrees of freedom so increased the computational time required to solve the transport problem, but this was unavoidable. The geometric properties of the throat nodes were chosen such that they had no impact on the hydraulic and diffusive conductance of the conduit, which were calculated before the throat nodes were added.

2.2. *Modeling of dilute solution transport*

Transport through the domain was modeled as advective–diffusive transport of a reactive solute. The pressure in each pore (and throat node) was first found by solving the flow problem assuming a fixed pressure drop across the domain (boundary conditions are outlined in section 2.3). The velocity in each throat was found using the computed pressures, then used to compute the advective–diffusive conductance values using the power-law scheme [34]. Finally, the advection–diffusion problem was solved to determine the concentration distribution in the domain in the presence of a reaction.

The conductance values were computed assuming cylindrical throats and spherical pore bodies, as shown in Fig. 2. The length of the pores, L_p, was found by subtracting the length of the intersection between a sphere and a cylinder from the radius of the pore. Due to the way that pore sizes were assigned they never overlapped, which helped to ensure the throat node procedure remained viable.

Given these assumptions, the total hydraulic conductance, G^h, of each pore-throat-pore conduit was computed as:

$$\frac{1}{G^h} = \frac{1}{g^h_{p,1}} + \frac{1}{g^h_t} + \frac{1}{g^h_{p,2}} \tag{1}$$

where $g^h_{p,i}$ for a sphere is [43,44]:

$$\frac{1}{g^h_{p,i}} = \frac{4\mu}{\pi r_p^3}\left(\frac{r_p L_p}{\left(r_p^2 - L_p^2\right)} + \tanh^{-1}\left(\frac{L_p}{r_p}\right)\right) \tag{2}$$

and g^h_t for a cylindrical throat is:

$$\frac{1}{g^h_t} = \frac{8\mu L_t}{\pi^2 r_t^4} \tag{3}$$

Similarly, the diffusive conductance, G^d, was found from:

$$\frac{1}{G^d} = \frac{1}{g^d_{p,1}} + \frac{1}{g^d_t} + \frac{1}{g^d_{p,2}} \tag{4}$$

where:

$$\frac{1}{g^d_p} = \frac{1}{D_A \pi r_p}\tanh^{-1}\left(\frac{L_p}{r_p}\right) \tag{5}$$

and:

$$\frac{1}{g^d_t} = \frac{L_t}{\pi r_t^2 D_A} \tag{6}$$

And the advective–diffusive conductance, G^{ad}, was found using the following power-law formulation [34]:

$$G^{ad} = \left(\frac{q_{ij}}{e^{Pe_{ij}} - 1}\right) \tag{7}$$

Pe_{ij} is the pore-scale Peclet number defined as:

$$Pe_{ij} = \frac{Q_{ij}}{A_t}\frac{L_t}{D_A} \tag{8}$$

where Q_{ij} is the volumetric flow between pores i and j. L_t and A_t are the length and cross-sectional area of the element, respectively, and D_A is the diffusion coefficient of the solute. Inserting the definition of the diffusive conductance and the fact that $Q_{ij} = G^h_{ij}\Delta P_{ij}$ yields the Peclet number for a conduit in terms of pre-computed conductance values and the calculated pressure values in each pore:

$$Pe_{ij} = \frac{G^h_{ij}}{G^d_{ij}}\Delta P_{ij} \tag{9}$$

The system was modeled at steady state so the mass balance around each node i can be expressed as:

$$\sum\nolimits_j \left(Q_{ij}C_{A,j} + G^{ad}\left(C_{A,j} - C_{A,i}\right)\right) = r_A \tag{10}$$

Writing Eq.(10) for every pore in the network yields a system of linear equations which must be solved simultaneously to determine the concentration in every pore.

The value of r_A in Eq.(10) was set to zero for pores where no reaction was occurring. In the throat nodes, the solute was consumed in a first-order heterogeneous reaction occurring at the solid–liquid interface in the throat nodes according to the standard rate expression:

$$r_A = k_r A_s C_{A,surf} \tag{11}$$

where k_r is the kinetic constant per unit area, A_s is the wetted surface area, and $C_{A,surf}$ is the concentration of the reactant at the surface. Only the bulk concentration is known after solving the system of equation defined by Eq.(10); however, since the reaction was assumed to occur at the solid–liquid interface the rate of mass transfer between the bulk fluid and the wall can be expressed as:

$$r_A = -k_L A_s\left(C_A - C_{A,surf}\right) \tag{12}$$

noting that the diffusion from the bulk to the surface corresponds to a consumption of A and hence a negative reaction rate. In Eq.(12), k_L is mass transfer coefficient. Equating these two expressions for the reaction rate and solving for r_A in terms of C_A yields:

$$r_A = \frac{k_r k_L}{k_L - k_r} A_s C_A \tag{13}$$

which provides the required expression for the rate of consumption of A in terms of the known concentration. The kinetic constant, k_r, was taken from Misaghian et al [1] for consumption of vanadium in a redox flow battery, while the mass transfer coefficient was computed from:

$$Sh = \frac{k_L D_t}{D_A} = 1.0 Re^{0.7} Sc^{0.33} \tag{14}$$

Sh was computed for each throat node and the throat diameter D_t was taken as the characteristic length. The surface area of each throat node was taken as the sum of the internal surface areas of the two neighboring throat segments which comprised the original throat. As mentioned above the velocity is not known in pores, yet this is where the mass balances and reactions are applied. Dividing throats into two segments separated by a "throat node" means that the velocity from the neighboring throat segment can be adopted as the velocity in each throat node. Finally, the total rate of reaction in the network was found by summing up the rate of consumption of species A in each pore using Eq. (10).

2.3. Boundary conditions

Constant pressure conditions were assigned to the inlet and outlet nodes of the network to solve for the pressure distribution and throat velocity. This is translated as a fixed pressure drop (Δp) across the domain. Additionally, at the inlet, the concentration (C_{in}) remained fixed, while an outflow boundary condition was imposed at the outlet pores, ensuring a zero gradient for the reactant species concentration. The specific values of boundary conditions used in this study are discussed in section 2.5 (System parameters).

2.4. Optimization algorithm

GA is a well-established optimization technique that draws inspiration from the principles of biological evolution, which find application in a wide range of fields, including optimization problems, machine learning, scheduling, and parameter tuning for machine learning models, among others. GA is a part of a broader class of algorithms known as evolutionary algorithms, which are designed to mimic the process of natural selection by adopting operators such as crossover, mutation, and selection to address computationally difficult or time-consuming problems. The sophisticated, nonlinear nature of reactive transport within porous media at the pore-level necessities the employment of gradient-free metaheuristic algorithms, such as GA, to seek the optimal PN morphology. In this work, a binary NSGA-II algorithm, a MOO variant of GA, is used to improve the conversion rate while concurrently minimizing pumping costs. NSGA-II is a mainstream choice for multi-objective optimization problems and has been successfully employed for various problems [45–48]. In this work, we opted for NSGA-II because of its robust and efficient algorithm for MOO problems. We acknowledge that other metaheuristic algorithms that might be advantageous for topological optimization of porous reactors, such as sailfish optimization (SFO)[49], whale optimization algorithm (WOA)[50], particle swarm optimization (PSO)[51], and multi-objective imperialist competitive algorithm (MOICA)[52] could be explored. However, a thorough comparison of these algorithms would require a comprehensive investigation that falls outside the scope of the present work.

As previously explained, the PN is generated based on a set of points residing on a background grid, forming the initial coordinates for potential pores. These initial coordinates undergo a relaxation function to determine the final pore coordinates within the PN. Each point in the problem grid corresponds to a potential pore within the PN, with the optimization problem controlling the presence or absence of these potential pores. Consequently, a Boolean value is assigned to each point, indicating whether the corresponding pore exists or not, and the optimization solutions are encoded as a Boolean vector, representing the existence or absence of candidate pores. Eliminating one pore may lead to the expansion of nearby pores, which facilitates the transportation of reactant species. Nevertheless, this action simultaneously affects the available reactive surface area. The algorithm begins with the Initialization step, wherein a set of n_{pop} initial solutions, referred to as the

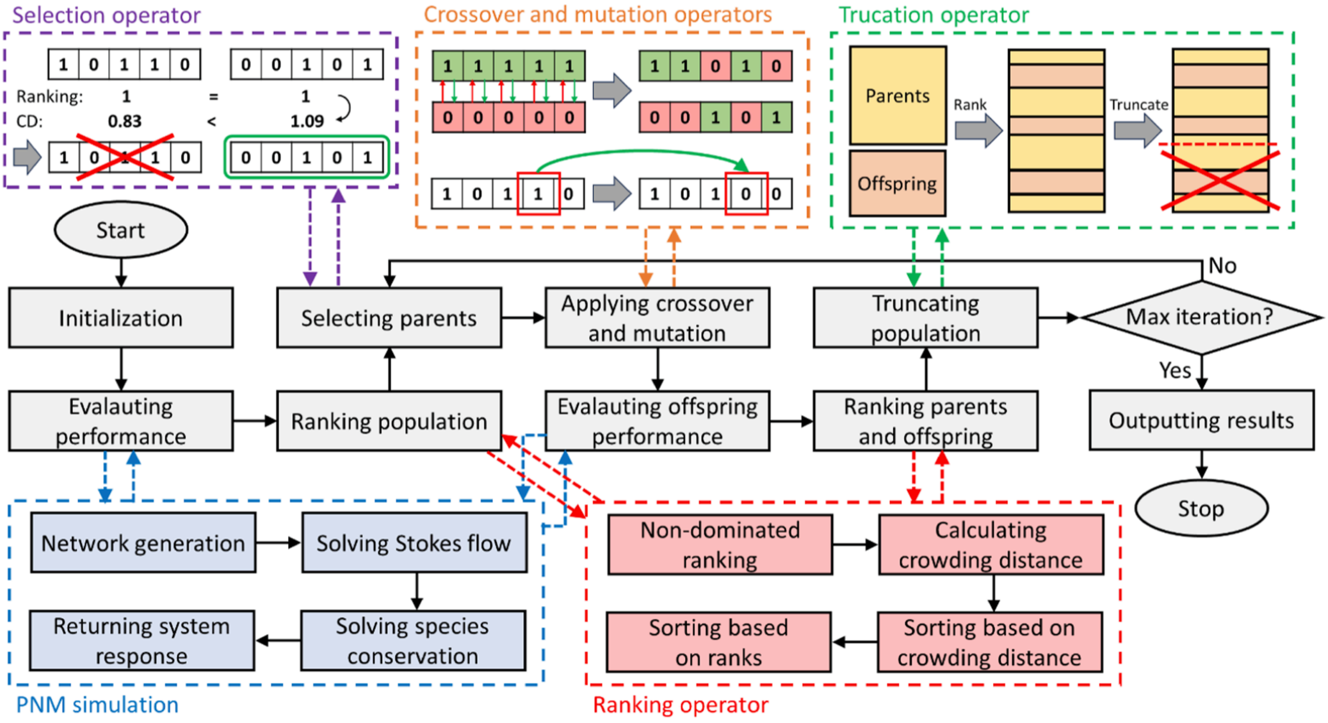

Fig. 3. Flowchart of optimization and simulation algorithms.

population or chromosomes, is randomly generated. Each individual within the population represents distinct combinations of potential pore existence, yielding a binary vector of length n_g, where n_g denotes the total number of points in the problem grid. The size of the grid is determined based on the number of points in each direction and the voxel size, which defines the spacing between neighboring grid points. Subsequently, the initial population undergoes iterative evolution, generating increasingly improved solutions over successive generations until convergence or a predefined termination criterion is satisfied. This study uses the maximum number of iterations as the termination criterion. The optimization problem is formulated as:

$$\begin{aligned} &\max_{V_g} \; F^1_{\text{obj}} = \sum\nolimits_{i=1}^{N_{\text{throat node}}} r_{A,i} \\ &\min_{V_g} \; F^2_{\text{obj}} = Q \times \Delta p \\ &\text{s.t.} \quad V_{g,j} \in \{0,1\} \quad \text{for} \quad j = 1,2,\cdots,n_g \end{aligned} \tag{15}$$

In which, F^1_{obj} and F^2_{obj} represents the total conversion rate and pumping power, respectively. As previously mentioned, F^1_{obj} is computed by summing the reaction rates in all throat nodes where reactions occur. Moreover, F^2_{obj} is determined by multiplying the overall reactor flow rate (Q) and the pressure drop (Δp). Q is evaluated by summing up the flow rate of fluid moving through the inlet pores, while Δp is dictated by the specified boundary condition. Also, the solution vector, denoted as V_g, represents the status of each pore in the problem grid. Following the initialization, NSGA-II proceeds to the fitness evaluation step. In this phase, the performance of each individual is assessed, by generating the corresponding PN, solving the governing equations, and calculating the conversion rate and pumping cost. It is worth noting that, in this study, population fitness evaluation is executed in parallel on several CPU cores. This parallelization significantly accelerates the calculation speed, allowing the algorithm to explore a wide search space and find high-quality solutions more rapidly. Subsequent to fitness evaluation, the algorithm performs a ranking process. It categorizes the population into different non-dominated fronts based on their fitness and dominance relationships. The first front contains Pareto optimal solutions, which are the best trade-offs between conversion rate and pumping cost and are not dominated by any other solution. In the crossover and mutation step, NSGA-II selects a pool of parent population via a binary tournament selection process for reproduction. These selected parents undergo a uniform crossover as well as mutation process to produce a new set of offspring. The crossover process combines data from two parent solutions, enabling the offspring to inherit their distinctive attributes, while the mutation operation makes random modifications to a single parent, thereby enriching exploration of the search space. Finally, in the selection and truncation step, the current population and offspring are merged to form a combined pool. Here, the algorithm applies ranking operation once again to select fittest individuals from the combined pool according to their ranking and crowding distance for the next generation. An overview of the optimization procedure is depicted in Fig. 3, with the primary operators briefly described as follows.

2.4.1. Initialization

In the initialization step, n_{pop} distinct PNs are generated randomly using Delaunay tessellation. As previously mentioned, each PN is represented by a solution vector, V_g, comprising n_g Boolean values that indicate presence or absence of each candidate pore in the final PN. To generate each V_g, first, a vector of random numbers between 0 and 1, with the same size (n_g), is produced using a uniform random distribution. Subsequently, each element in this vector is compared to a chosen threshold value. Values below the threshold indicate the existence of the corresponding pore, while values exceeding the threshold signify the absence of the potential pore. As the initial random numbers (between 0 and 1) were generated using a uniform random distribution, tuning the threshold value approximately determines the overall percentage of pores that exist in the final PN. For instance, choosing a threshold with an extreme value of one will lead to the presence of all potential pores from the background in the final PN (see Fig. 1a). It is well-known that the efficiency of GA is significantly influenced by the quality and diversity of the initial population [53]. To ensure appropriate diversity, a range of threshold values is considered based on linear spacing between 0 and 1, in accordance with n_{pop}. This initialization strategy ensures the presence of a diverse range of design solutions in the initial population, encompassing configurations with low, medium, and high numbers of pores. In other words, out of the entire intial populations generated in this study, the threshold value for each one was different, ranging linearly from 0 to 1. Hence, among the initial populations, there existed design solutions with various numbers of pores. From this perspective, we started with generating populations with a “vector of random continuous variables”, but then converted this to a “binary vector” using the threshold value.

2.4.2. Population ranking front

NSGA-II [54,55] employs a non-dominated sorting operator to rank the individuals of a population in a case with multiple objectives. The initial step in this operator is non-dominated sorting, which classifies individuals into distinct fronts based on their dominance relationships. Dominance is determined by comparing the objective function values of two individuals. If one individual is superior in at least one objective and not worse in any other, it is considered dominant. For instance, in this study, conversion rate and pumping cost are treated as two conflicting objectives. A solution exhibiting a higher conversion rate and lower pumping cost consistently dominates any alternative solutions characterized by lower conversion rates and higher pumping costs. However, in scenarios where both the conversion rate and pumping cost of two solutions are either simultaneously higher or lower compared to each other, mutual domination does not occur, and these solutions are categorized within the same class (or front). This process organizes individuals into a series of fronts, where the first front consists of non-dominated individuals, the second front contains individuals dominated only by those in the first front, and so on. After non-dominated sorting, the next step is to calculate the crowding distance (CD) for each individual within a front. CD reflects the density of individuals in the objective space, helping to maintain diversity in the population. It is calculated by considering the distances between an individual and its neighboring individuals along each objective dimension. Individuals with higher CDs are preferred as they contribute to a more evenly distributed Pareto front. The final sorting of the entire population is a two-step process: first, individuals are sorted based on their crowding distance in descending order, ensuring that individuals with greater CDs are prioritized. The second sorting is the front ranking, arranging individuals based on their front ranking. This sequential sorting based on CD and front ranking guarantees a systematic arrangement of population according to dominance. In tied rankings, priority is assigned by considering their CD values. This dual-criteria sorting mechanism ensures a meticulous organization of individuals within the population, promoting a comprehensive and balanced exploration of the solution space. In each generation, following the arrangement of the merged parent and offspring populations through the previously outlined procedure, the top n_{pop} individuals survive and advance to the subsequent generation during the truncation process. This mechanism ensures that only the fittest individuals, determined by their performance in the optimization objectives, pass to the next generation, fostering a continuous progression of the population toward superior solutions.

2.4.3. Binary tournament selection

The optimization process uses a binary tournament method to select parents for the reproduction of offspring. This method randomly samples two individuals from the population and evaluates their dominance relationship, ultimately selecting the parent with a superior front

Table 1
Optimization algorithm parameters.

Optimizer parameter	Value
Population size (n_{pop})	1200
Crossover ratio (p_c)	0.85
Mutation ratio (p_m)	0.05
Mutation rate (r_m)	0.1

ranking and CD. This strategic approach ensures that all individuals have an opportunity to participate in reproduction, thereby promoting overall diversity. However, fitter individuals are granted a higher probability of passing on their genomes to the subsequent generations, aligning with the principle of biological evolution and natural selection. Further information regarding this selection scheme can be found in the literature [56,57].

2.4.4. *Crossover*

In the present study, a uniform crossover operator is utilized to generate new PNs by exchanging genetic information between pairs of parent networks. The selection of parent networks is performed through a binary tournament. The number of reproduced offspring from the crossover process is determined by a given crossover ratio (p_c) and is calculated by $2 \times \left\lceil \frac{p_c \times n_{pop}}{2} \right\rceil$. Each PN is represented by a vector of binary genome, and the uniform crossover operates independently on each genome (see Fig. 3). Notably, a pair of parents gives rise to two children, with the decision on the inheritance of genomes from each parent to each child being dictated by a uniform random distribution.

2.4.5. *Mutation*

The mutation operator introduces random changes into the genetic makeup of solutions, fostering diversity in the population and promoting exploration within the search space. First, a subset of $\lceil p_m \times n_{pop} \rceil$ individuals are randomly selected for mutation from the parents' pool, where p_m is a specified mutation ratio. The severity of mutation is then dictated by the mutation rate (r_m), with $\lceil r_m \times n_g \rceil$ genomes being flipped at random positions (see Fig. 3) using a "bit mutation" operator. This targeted alteration in genetic information introduces variability among the individuals, contributing to the algorithm's capacity for effective exploration of the solution space. This inherent randomness is fundamental for avoiding premature convergence and promoting the continued exploration of the search space. The introduction of slight variations ensures that the optimization algorithm is not confined to a narrow region of the solution space and is better equipped to discover diverse and potentially optimal solutions. The values of algorithm parameters are given in Table 1. The number of generations (iterations) in optimization is specified based on the size of search space. It is also noteworthy that "crossover ratio" and "mutation ratio" indicate the proportion of the population that undergoes crossover and mutation operations, respectively. Once an individual is selected for mutation, only a portion of its genes undergoes mutation. "Mutation rate" defines the severity of the mutation by specifying this proportion.

2.5. *System parameters*

The proposed framework is employed to optimize the PN topology of an ADR porous reactor. This reactor facilitates the transport of a dilute solution through advection–diffusion mechanisms, extending from the inlet to outlet boundaries, while simultaneously an arbitrary solute species A is reacted in presence of active surface area. Depending on the configuration of parameters, the system may exhibit characteristics of either kinetic or hydraulic sluggishness. The optimization process is designed to yield a tailored PN topology that improves system performance by achieving a balanced compromise between transport and rate phenomena. This involves proper control of both surface area and permeability through alternation of PN morphology. The properties of the solution and solute are adopted from literature for vanadium ion redox reaction in a VRFB. The values of these properties as well as the operating conditions (boundary conditions) are presented in Table 2. Although the developed model does not involve all phenomena occurring in a VRFB, the reaction constant, k_r, is estimated according to the Butler-Volmer kinetics assuming a constant overpotential and a largely polarized condition (only forward reaction) as described below.

$$k_r = k_0 \exp\left(\frac{\alpha F}{RT}\eta\right) \tag{16}$$

In this equation, α, T, η, F, and R are charge transfer coefficient, temperature, overpotential, Faraday's constant, gas constant, respectively.

Table 2
System properties and operational conditions.

Parameter	Unit	Value / range
Grid shape	–	50 × 13 × 13
Voxel size (d)	μm	40
Grid dimensions	mm^3	2 × 0.52 × 0.52
Number of candidate pores	–	8450
Solution density (ρ) [1]	$\mathrm{kg\,m^{-3}}$	1350
Solution viscosity (μ) [1]	Pa s	0.005
Solute diffusion coefficient (D_A) [1]	$\mathrm{m^2 s^{-1}}$	3.9×10^{-10}
Kinetic constant per unit area (k_0) [1]	$\mathrm{m\,s^{-1}}$	5×10^{-7}
Solute concentration (C_{in}) [1]	$\mathrm{mol\,m^{-3}}$	600
Charge transfer coefficient (α) [1]	–	0.5
Temperature (T)	K	298
Pressure drop (Δp)	Pa	400
Overpotential (η)	V	0.3

3. Results and discussion

A 3D background grid with shape 50 × 13 × 13 and spacing of 40μm is assumed as the PN design domain. The optimization process aimed to identify the optimal PN morphology within this $2 \times 0.52 \times 0.52\mathrm{mm}^3$ lattice, toggling candidate pores on and off under the assumption of flow occurring in the longitudinal direction (2mm). Following the determination of the presence or absence of each potential pore in the configuration, the PN was constructed, and simulations were conducted using OpenPNM, as described in the preceding sections. This iterative procedure was repeated for 1000 generations, during which the optimizer generated an improved set of Pareto optimal PN topologies in each iteration. The parent population pool initially consisted of 1200 solutions and 1080 new offspring were reproduced through crossover and mutation processes ($n_p \times (p_c + p_m) = 1200 \times (0.85 + 0.05) = 1080$). Next, the objective function was evaluated, resulting in the model being solved over one million times in total during the optimization process. Such an ultra-large optimization with high resolution was only manageable through a cost-effective modeling method like PNM.

Fig. 4(a) illustrates the history of Pareto fronts of dual objectives over all generations, showing reaction rate and pumping cost of various non-dominated solutions. As optimization progressed, enhanced PN morphologies were generated, leading to higher conversion rates and lower pumping costs. It is noteworthy that all points on the Pareto graph of each generation can be considered as potential optimal points, depending on the trade-off between reaction rate and pumping power. If minimal pumping cost is crucial, the point on the bottom-left corner of the Pareto front can be chosen as the optimum design. Conversely, if maximal conversion rate is the goal, the point on the opposite extreme could be selected. The "*ideal point*" on this graph lies on the top-left corner, where a very high reaction rate could be achieved with minimal pumping requirements. The Pareto optimal solutions in this figure tend toward that *ideal point*. For instance, comparing points A_1 and B_1, the ending points of the Pareto fronts after and before optimization (generations 1000 and zero), reveals a 280% increase in reaction rate

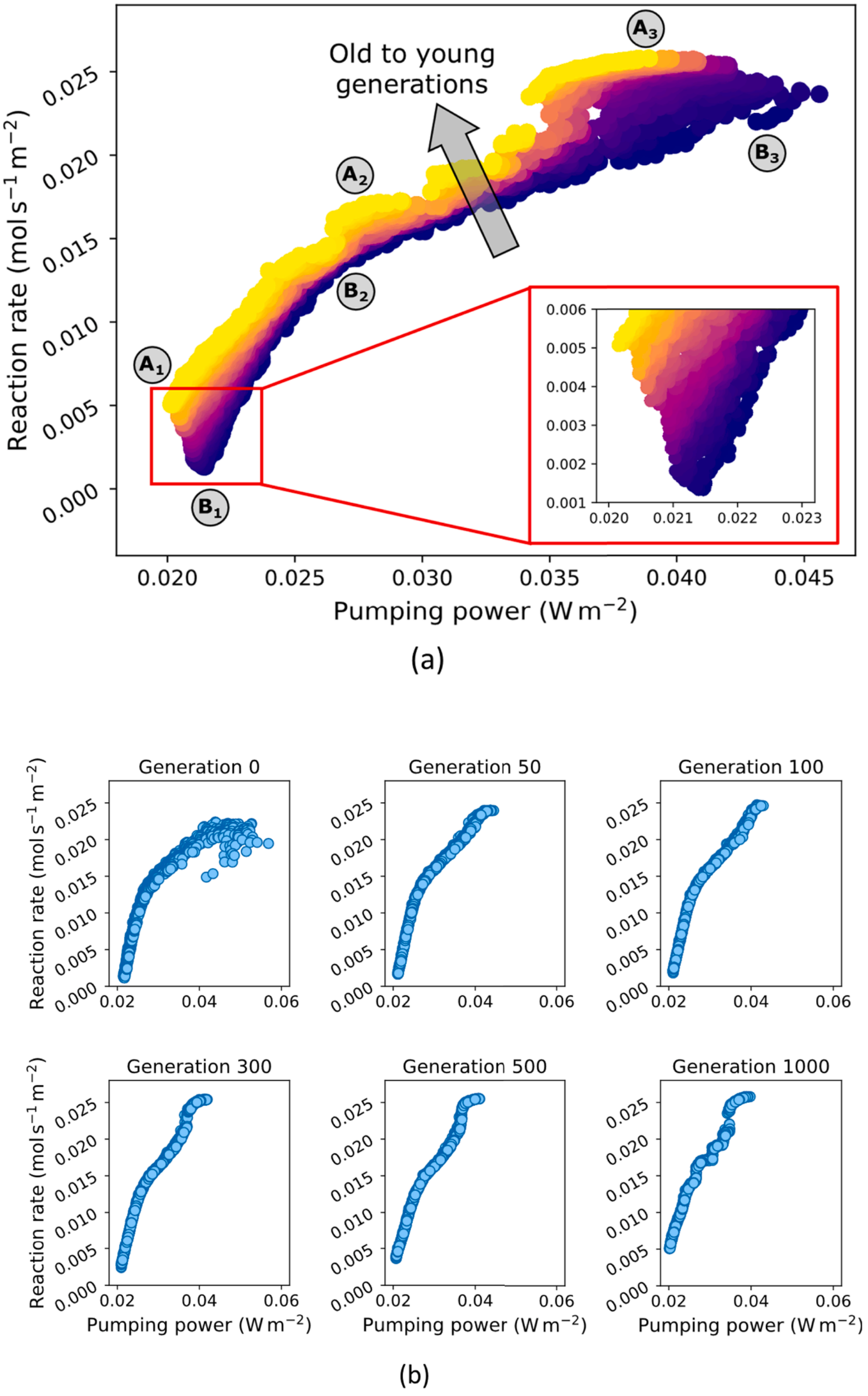

Fig. 4. History of (a) Pareto fronts, (b) entire population, and (c) hypervolume over optimization process. In (a), each color spectrum represents Pareto optimal solutions of one generation, from dark purpule for generation zero and yellow for generation 1000. (For interpretation of the references to color in this figure legend, the reader is referred to the web version of this article.)

accompanied by a 6% reduction in pumping cost. Such a significant elevation in the conversion rate, along with an appreciable reduction in hydraulic requirements, was only achievable through a robust optimization process that led to proper configuration of the pores in the final PN. Furthermore, comparing points A_3 and B_3, situated at the other end of Pareto fronts of the optimal and initial generations (see Fig. 4(a)), shows a similar trend. The reaction rate increased by 15.2%, and pumping power decreased by 11.3%. Choosing any points between the two ends on the Pareto front depends on practical constraints and the trade-off between the two objectives. For instance, in a practical application such as VRFB, the net generated power (i.e. the difference between cell and pumping power) can determine a proper trade-off between the two objectives. In such cases, the framework presented in this paper can be utilized with a single-objective optimization algorithm, such as GA, to produce innovative PN with improved performance. However, in the absence of any particular trade-off, points A_2 and B_2 are

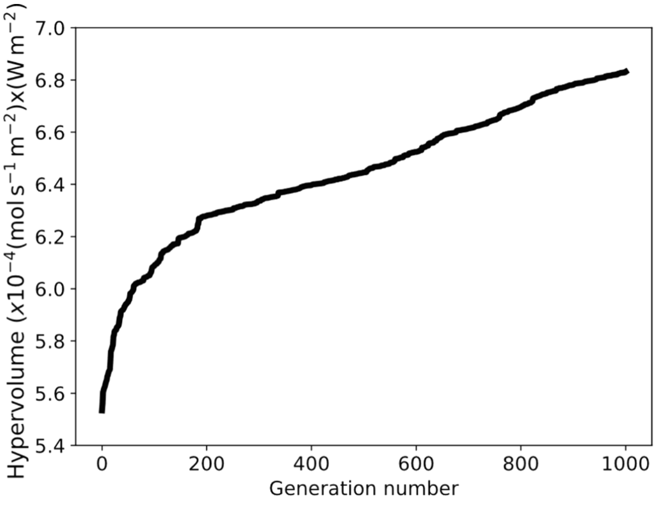

(c)

Fig. 4. (*continued*).

Table 3
Comparison of the results between the three representative cases before and after optimization.

Parameter	Cases					
	A_1	**A_2**	**A_3**	**B_1**	**B_2**	**B_3**
Reaction rate ($\times 10^{-3}$ mol s^{-1}m^{-2})	5.06	16.7	25.8	1.33	12.2	22.4
Pumping power ($\times 10^{-2}$ W m^{-2})	2.01	2.74	3.89	2.15	2.60	4.39
Number of pores	7082	4540	3198	7847	5407	3084
Minimum pore diameter (μm)	23.5	23.3	23.3	26.0	21.8	23.6
Maximum pore diameter (μm)	53.9	67.7	88.0	46.4	60.5	116.7
Average pore diameter (μm)	30.3	31.7	32.6	30.6	31.4	32.8
Average throat diameter (μm)	16.7	17.1	17.7	16.6	16.9	17.7
Superficial velocity (mm s^{-1})	0.194	0.263	0.374	0.206	0.250	0.422
Porosity (−)	0.379	0.423	0.473	0.392	0.410	0.475
Permeability (D)	4.84	6.58	9.36	5.16	6.24	10.55
Specific surface area (m^{2}m^{-3})	8273	27086	36641	1827	19841	29882

chosen for the sake of comparison in this study. These points have a median pumping power among all solutions in their corresponding Pareto front. A quantitative comparison of these three representative points before and after optimization is reported in Table 3. A more detailed comparison of the PN of optimal solutions is provided later in this study.

Moreover, Fig. 4(b) and (c) show the convergence history of optimization process in terms of entire population and hypervolume, respectively. As shown in Fig. 4(b), it is evident that the entire population, over generations, improved in both reaction rate and pumping cost, shifting toward the *ideal point*. This figure also confirms that while the randomly generated population at generation zero is spread on the plot surface, the solutions in subsequent generations become more converged. As a post-processing step, optimization convergence is tracked using a hypervolume indicator [58], shown in Fig. 4(c). In this case, the hypervolume is the area under the Pareto plot in each generation with respect to a reference point. The reference point, assumed in this study as (pumping cost, reaction rate) = (0.0527W m^{-2}, 0), represents a relatively poor solution dominated by all Pareto solutions. The incremental trend of hypervolume plot in Fig. 4(c) indicates the improvement of Pareto front over generations. It is noticeable that the hypervolume indicator increased sharply in the first 200 generations, signifying rapid improvement at the beginning of the optimization

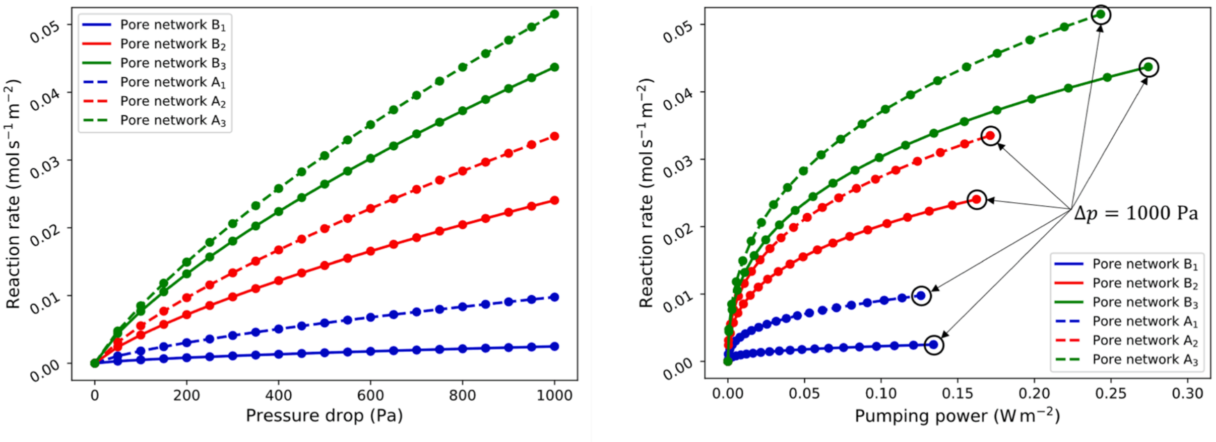

(a) (b)

Fig. 5. (a) Pressure drop-reaction rate and (b) pumping power-reaction rate performance curves of representative PMs before and after optimization.

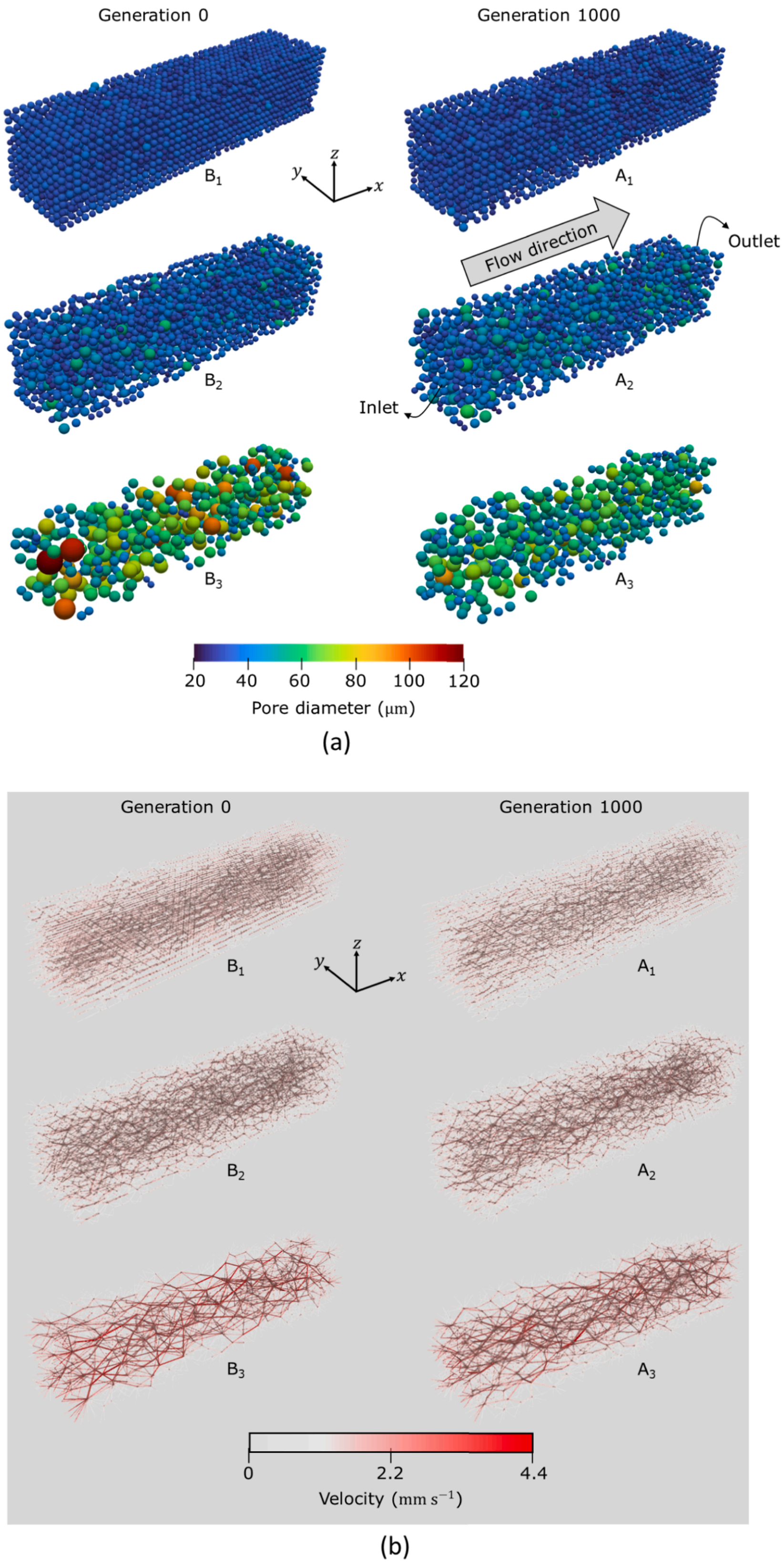

Fig. 6. Comparison of representative PNs before and after optimization. (a) pore size, (b) solution velocity, and (c) bulk concentration distribution.

process, followed by a gradual slowing down as the optimization reaches convergence.

While the optimization was conducted at a fixed pressure drop ($\Delta p = 400\mathrm{Pa}$), a more comprehensive understanding was sought by investigating the porous reactor's performance before and after optimization for a wide range of pressure drops. Fig. 5(a) and (b) illustrate pressure

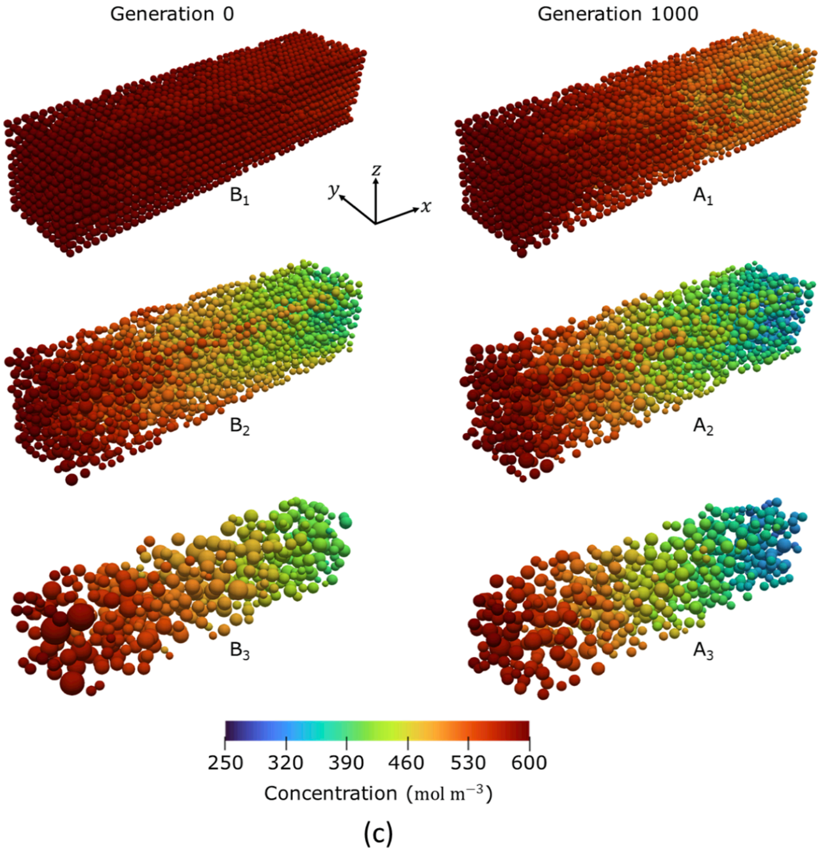

Fig. 6. (*continued*).

drop and pumping power versus reaction rate, respectively, for six representative PNs. Comparing the conversion rate of PNs after optimization (points A) with their corresponding networks before optimization (points B), as depicted in Fig. 5(a), clearly demonstrates the superior performance of optimal PNs across various pressure drops. Furthermore, it is observed that the pressure drop-reaction rate curve of A_3 shows the best performance among all other PNs in Fig. 5(a), even when compared to PNs A_1 and A_2. However, it is important to note that while the reaction rate of A_3 is higher than other PNs at the same pressure drop, this higher conversion rate comes at the cost of a higher pumping cost, as confirmed by the pumping power-reaction rate curves shown in Fig. 5(b). All curves in this figure are plotted for a pressure drop up to 1000Pa, similar to Fig. 5(a). Clearly, A_3 demands a higher hydraulic power compared to A_1 and A_2. Moreover, A_3 has the capability to cover a wider range of pumping cost for a given pressure drop range, thanks to its higher permeability, which is not achievable by other PNs. Similarly, with a common pumping cost, A_3 exhibits a higher conversion rate (see Fig. 5(b)), but this is only possible with different pressure drops. Therefore, the choice of the best PN depends on the application constraints and the trade-off between the reaction rate and pumping cost.

Fig. 6 demonstrates the morphology and simulation results of the initial and optimal representative PNs without throat nodes. A closer look at Fig. 6(a) reveals that PNs B_1 and A_1 contain a higher number of pores compared to B_3 and A_3, as quantitatively reported in Table 3. This condensed configuration leaves less space for the pores to grow in the given design domain, resulting in many relatively small pores. In contrast, by deleting some potential pores, the remaining pores in PNs B_3 and A_3 had the chance to become larger, with some pores exhibiting a diameter larger than 100μm in B_3. Comparing the PNs before and after optimization illustrates how the network topologies evolved over the optimization process.

Additionally, in a PNM, throats serve as pathways for fluid transport. As explained earlier, the throat diameter is determined based on the minimum diameter of its neighboring pores. Therefore, a PN with larger pore diameters features larger throats on average, facilitating fluid flow. This is confirmed by Fig. 6(b), which illustrates the velocity magnitude in the bundle of throats, and the superficial velocity stated in Table 3. According to Eq.(3), the hydraulic conductance of a cylindrical throat is proportional to the fourth power of its radius. Hence, enlarging a throat can greatly increase the flow rate passing through it with a fixed pressure difference. Since the reaction rate depends on the local concentration of active species, a fast delivery of reactant species may lead to a higher total conversion rate. However, it is noteworthy that an excess hydraulic conductance and flow rate may be obtained at the cost of higher pumping power and lower reactive surface area, without contributing to the total reaction rate. Therefore, during the evolution process from B_3 to A_3, for instance, the optimizer favored changing the topology so that very large pores were replaced with several smaller ones. In ADR systems, the mass transfer coefficient plays a key role in determining the rate of reactant consumption. According to Eq.(14), k_L is a function of Reynolds number, which itself depends on the fluid velocity. Therefore, even a concentrated solution with a high bulk concentration may not result in rapid chemical reaction if the convective fluid velocity is low. For example, the concentration distribution of PN A_1 in Fig. 6(c) indicates that the species concentration in the pores near outlet boundary is almost equal to those near inlet boundary. Due to the slow fluid flow in this network, the mass transfer coefficient is so low that a considerable portion of the active species exits the reactor without undergoing reaction. In contrast, the higher velocities observed in PNs A_2 and A_3 (refer to superficial velocity values in Table 3 and velocity magnitude in Fig. 6(b)) promote enhanced species transport from the bulk solution to the solid surface, resulting in a faster consumption of active species. The elevated reaction rate in A_3 corresponds to a lower

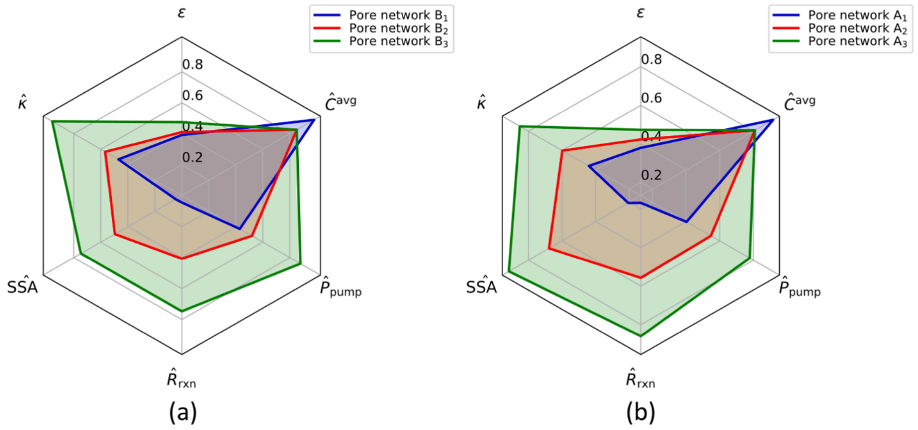

Fig. 7. Macroscopic structural and performance properties of the representative PNs: (a) before optimization and (b) after optimization.

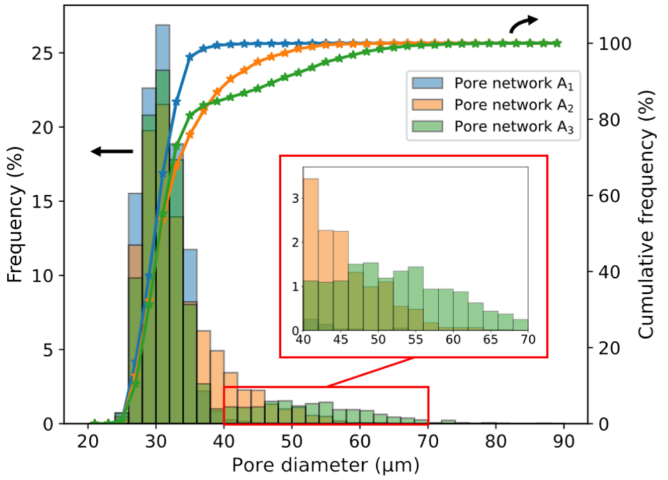

Fig. 8. The pore size distribution of optimized PNs, displaying pore diameter frequency and the cumulative frequency in terms of percentange (%).

bulk concentration in regions near the outlet, with the minimum concentration reaching approximately $284 \mathrm{mol\,m^{-3}}$.

However, the fluid velocity, prescribed by the network hydraulic conductance, is not the sole determining factor in the overall performance of a PN. Another critical parameter in this multi-objective optimization problem is the active surface area. In a PNM, this value depends on the definition of the surface area and the geometrical assumptions of the network. As discussed earlier, in this study, the reactive surface area of each “throat node,” where the chemical reaction occurs, is assumed to be equal to the internal surface area of throat with which it is associated. The surface area of the pore bodies was excluded since the fraction of its area to associate with each throat is not easily determined. This assumption is justified on geometrical grounds because the internal surface area of a pore is reduced by the opening created by each intersecting throat, so the internal surface areas are quite low. In fact, the internal surface area of all pores in network A_3 was $1.81 \times 10^{-6} \mathrm{m}^2$, while the throat surface area was $1.05 \times 10^{-5} \mathrm{m}^2$, so on average we can expect ignoring this surface area only affects the active surface area by 17%. This assumption is also supported on physical grounds since the fluid velocity in pores is lower than throats so the reaction will be more mass transfer limited, thus would contribute relatively little reaction to each throat.

The radar charts in Fig. 7 display the topological characteristics and performance of the representative PNs before and after optimization. Here, ε, κ, SSA, R_{rxn}, P_{pump}, and C^{avg} denote porosity, permeability, specific surface area, reaction rate, pump power, and average bulk concentration, respectively. The values with a hat symbol (ˆ) are normalized with respect to a common reference value, converting them all between 0 and 1. Porosity, permeability, and SSA values are calculated using OpenPNM for each network. In this context, SSA is defined as the ratio of the wetted surface area to the volume of the solid phase. Comparing the results before (B points) and after (A points) optimization reveals a considerable increase in SSA value for all three networks. The enhancement of SSA, resulting from an improved network topology, contributes to the increment of the reaction rate in all PNs. Additionally, permeability serves as an index of the overall network hydraulic conductance. Since the pressure drop was kept fixed during the optimization process, the pumping cost depends solely on permeability. For instance, the lower permeability (9.36D vs. 10.55D, 11.3% decrease) and higher SSA ($36641 \mathrm{m^2 m^{-3}}$ vs. $29882 \mathrm{m^2 m^{-3}}$, 22.6% increase) of A_3 compared to B_3 helped reduce the pumping requirement and increase the reaction rate after optimization.

The pore size distribution of the optimized networks (represented by points A) is illustrated in Fig. 8. As depicted, the histogram of PN A_3 is right shifted compared to the other networks, indicating the presence of larger pores. PN A_3 comprises a number of pores exceeding a diameter size of 40μm, a characteristic not observed in PN A_1. Larger pores are associated with larger throats connected to them. As previously discussed, larger throats exhibit higher hydraulic conductivity, leading to an elevated Reynolds number. This, in turn, enhances mass transfer between the bulk fluid and the solid–liquid interface, increasing the likelihood of reactant species undergoing reaction before leaving the electrode. Moreover, the larger pores distributed in the longitudinal direction (see Fig. 6(a)) facilitate the rapid delivery of reactants to regions far from the inlet and therefore mitigate significant concentration depletion. In contrast, as demonstrated in Fig. 8, PN A_1 exhibits a more uniform pore size distribution within a condensed configuration.

Finally, the 3D rendered representations of the solid-phase porous reactor, derived from the dimensions of pores and throats across six representative PNs, are presented in Fig. 9. This figure showcase how the predicted networks can be turned into a solid object. Some numerical analysis of these images are provided in the **Supplementary Information**. While manufacturability of these tailored designs currently relies on the accuracy and resolution limitations of existing technologies, it is envisoned that the ongoing advancements in additive manufacturing methods, such as projection micro stereolithography [6], offer promising avenues for fabricating such intricate structures with greater precision and efficiency. The proposed PNM-NSGA optimization framework proves capable of tailoring innovative microstructures at a pore-scale with high resolution, encompassing multi-physics considerations without relying on a cubic lattice. Further studies are imperative to explore the impact of various operating and structural parameters, the trade-off between objectives, and the incorporation of additional physics

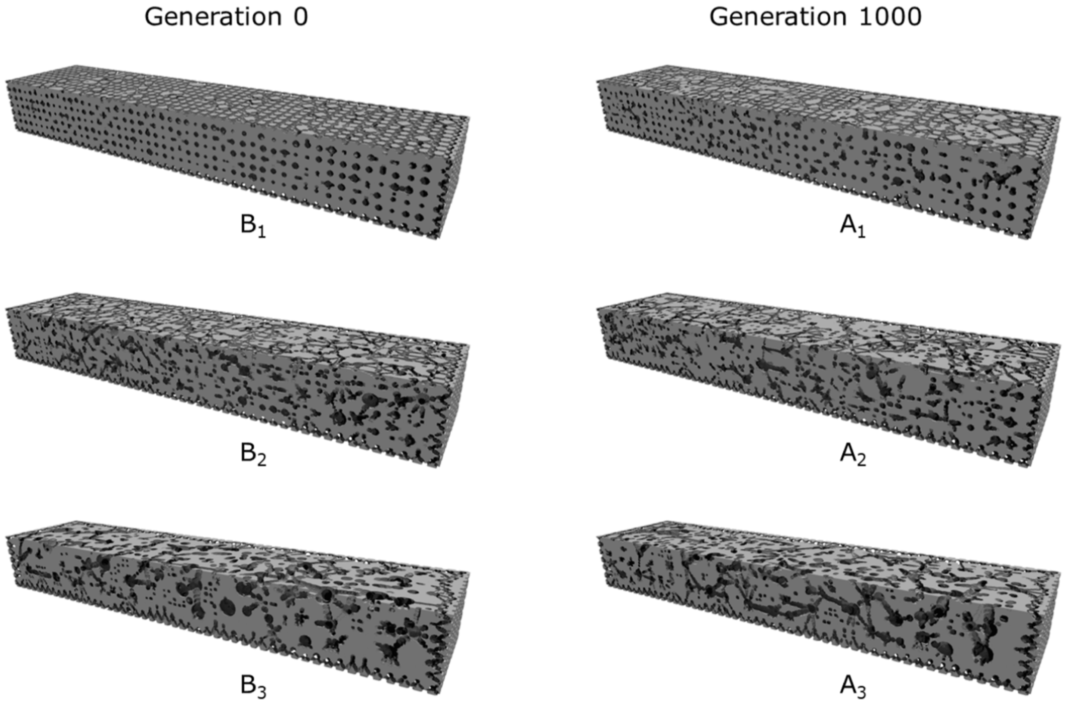

Fig. 9. Solid-phase porous skeleton of networks generated by PNM-NSGA framework. The grey is solid phase.

and more complicated reaction kinetics.

4. Conclusions

This study presents a robust framework for the large-scale optimization of porous reactors by integrating PNM with the NSGA-II algorithm. The proposed approach capitalizes on the computationally efficient nature of PNM to model reactive transport in a porous reactor at the pore scale. It employs the NSGA-II multi-objective optimizer to enhance the porous network morphology, aiming to maximize conversion rates and minimize hydraulic requirements. Distinguished from previous studies, the proposed framework introduces the idea of background grid, and utilizes Delaunay tessellation as well a relaxation operation to provide greater freedom for the pore coordinates. Formulating the problem as a multi-objective optimization offers a versatile framework applicable to various applications with contradictory objectives, eliminating the need for a specific trade-off.

The proposed PNM-NSGA framework was applied to optimize the microstructure of a $2 \times 0.52 \times 0.52\,\mathrm{mm}^3$ porous reactor, coupling advection–diffusion phenomena with a first-order chemical reaction. To account for the impact of convective flow on the mass transfer coefficient between bulk liquid and the solid–liquid interface, “throat nodes” were introduced to the developed PNM where a local mass transfer coefficient was incorporated into the reaction term. The algorithm generated a range of Pareto optimal solutions for various pumping costs. Comparison of the optimal solution with the lowest pumping cost on one end of the Pareto front with its corresponding PN in the initial generation revealed a significant 280% increase in reaction rate accompanied by a 6% decrease in pumping cost. This improvement is attributed to the precise placement and sizing of pores in the designated design domain. In the absence of a specific trade-off between objectives, three distinct optimal solutions were selected from different regions of the Pareto front and thoroughly compared. The presented methodology can be used for designing porous reactors with pore-scale resolution in various applications, such as electrodes for electrochemical energy devices (e.g., flow batteries, fuel cells, and electrolyzers) and catalytic reactors. With advancements in additive manufacturing techniques and manufacturability resolution, it is envisioned that these robust algorithmic methods will have broad application in generating high-performance porous reactors. Further exploration is necessary to extend this framework to accommodate additional physics, enhance its degree of freedom, and reduce computational costs. Additionally, more investigation is required concerning the manufacturability of the generated network topologies.

CRediT authorship contribution statement

Mehrzad Alizadeh: Writing – review & editing, Writing – original draft, Visualization, Software, Resources, Project administration, Methodology, Investigation, Funding acquisition, Formal analysis, Data curation, Conceptualization. **Jeff Gostick:** Writing – review & editing, Writing – original draft, Visualization, Supervision, Software, Resources, Methodology, Investigation, Funding acquisition, Formal analysis, Conceptualization. **Takahiro Suzuki:** Writing – review & editing, Investigation, Formal analysis, Data curation. **Shohji Tsushima:** Writing – review & editing, Supervision, Resources, Investigation, Funding acquisition, Formal analysis, Conceptualization.

Declaration of competing interest

The authors declare that they have no known competing financial interests or personal relationships that could have appeared to influence the work reported in this paper.

Data availability

No data was used for the research described in the article.

Acknowledgements

This work was supported by Grant-in-Aid for JSPS Fellows number 22KJ2198, JSPS KAKENHI Grant number 21H04540, and JSPS Invitational Fellowship for Research in Japan number L23534.

Appendix A. Derivation of hydraulic conductance for a sphere

The hydraulic conductance of pore segment, g_p^h, as expressed in Eq.(2) can be derived via two methods. First, the simpler approach is explained as follows. Since the cross section of a sphere is not constant when moving from a pole to the center, the Hagen-Poiseuille model cannot be used for evaluation of hydraulic conductance. Assuming that the part of the sphere from center to L_p (see Figure A–1) consists of infinite number of infinitesimal cylinder-like rings in series, the Hagen-Poiseuille model can be used to calculate the overall hydraulic conductance by taking an integral of the hydraulic resistivity over this portion as follows:

$$\frac{1}{g_p^h} = \int_0^{L_p} \frac{8\mu dx}{\pi r^4(x)} \tag{A1}$$

where x denotes the distance from center of the sphere. The radius of an infinitesimal ring depends on x and is given by:

$$r(x) = \sqrt{r_p^2 - x^2} \tag{A2}$$

By inserting Eq.(A–2) into Eq.(A–1) and calculating the integral, the overall hydraulic conductivity is expressed as:

$$\frac{1}{g_p^h} = \int_0^{L_p} \frac{8\mu dx}{\pi\left(r_p^2 - x^2\right)^2} = \frac{4\mu}{\pi r_p^3}\left[\frac{r_p L_p}{r_p^2 - L_p^2} + \tanh^{-1}\left(\frac{L_p}{r_p}\right)\right] \tag{A3}$$

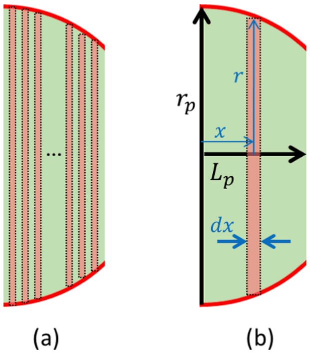

Fig. A1. Representation of sphere segment in a pore-throat-pore conduit. (a) shows assumption of infinite number of differential rings in series, and (b) shows the geometric dimensions of an infinitesimal ring.

A more comprehensive and robust derivation could be obtained based on the approximate analytical solution of laminar, single-phase flow in a gradually-varying channel of arbitrary cross-section that was previously studies by Bahrami and coworkers [43,44]. They showed that the pressure drop in a conduit with slowly changing cross-section is expressed by:

$$-\frac{1}{Q}\left(\frac{dp}{dx}\right) = \mu\left[16\pi^2\left(\frac{I_p^*}{A^2(x)}\right) - \frac{2\rho Q}{\mu}\left(\frac{dA(x)/dx}{A^3(x)}\right)\right] \tag{A4}$$

in which I_p^* is the specific polar moment of inertia and $A(x)$ is the cross-section area. For a circular cross-section, $A(x)$ is given by:

$$A(x) = \pi r^2(x) = \pi\left(r_p^2 - x^2\right) \tag{A5}$$

The first and second terms on the right-hand-side of Eq.(A–4) correspond to frictional and inertial losses, respectively. Given the assumption that the cross-section area is changing gradually ($dA(x)/dx \rightarrow 0$), the frictional loss is typically substantially more than the inertial loss and therefore the second term could be neglected. The total pressure drop can be computed by integrating Eq.(A–4) over the length of L_p after ignoring the inertial term as follows:

$$\frac{\Delta p}{Q} = 16\pi^2\mu\int_0^{L_p} \frac{I_p^*}{A^2(x)}dx \tag{A6}$$

Given the definition of hydraulic conductance as the ratio of the volumetric flow rate to the pressure drop ($g_p^h = Q/\Delta p$) and knowing the specific polar moment of inertia of a circle is $\frac{1}{2\pi}$, the hydraulic conductance is derived as:

$$\frac{1}{g_p^h} = 16\pi^2\mu\int_0^{L_p}\frac{(1/2\pi)}{\left[\pi\left(r_p^2 - x^2\right)\right]^2}dx = \frac{4\mu}{\pi r_p^3}\left[\frac{r_pL_p}{r_p^2 - L_p^2} + \tanh^{-1}\left(\frac{L_p}{r_p}\right)\right] \tag{A7}$$

Appendix B. Supplementary data

Supplementary data to this article can be found online at https://doi.org/10.1016/j.compstruc.2024.107452.

References

[1] Misaghian N, Sadeghi MA, Lee KM, et al. Utilizing Pore Network Modeling for Performance Analysis of Multi-Layer Electrodes in Vanadium Redox Flow Batteries. J Electrochem Soc 2023;170:070520. https://doi.org/10.1149/1945-7111/ace554.

[2] Sun Y, Polani S, Luo F, et al. Advancements in cathode catalyst and cathode layer design for proton exchange membrane fuel cells. Nat Commun 2021;12:5984. https://doi.org/10.1038/s41467-021-25911-x.

[3] Kočí P, Novák V, Štěpánek F, et al. Multi-scale modelling of reaction and transport in porous catalysts. Chem Eng Sci 2010;65:412–9. https://doi.org/10.1016/j.ces.2009.06.068.

[4] Zhu J, Wu P, Chao Y, et al. Recent advances in 3D printing for catalytic applications. Chem Eng J 2022;433:134341. https://doi.org/10.1016/j.cej.2021.134341.

[5] Ambrosi A, Pumera M. 3D-printing technologies for electrochemical applications. Chem Soc Rev 2016;45:2740–55. https://doi.org/10.1039/C5CS00714C.

[6] Reale Batista MD, Chandrasekaran S, Moran BD, et al. Design and additive manufacturing of optimized electrodes for energy storage applications. Carbon 2023;205:262–9. https://doi.org/10.1016/j.carbon.2023.01.044.

[7] Capel AJ, Rimington RP, Lewis MP, Christie SDR. 3D printing for chemical, pharmaceutical and biological applications. Nat Rev Chem 2018;2:422–36. https://doi.org/10.1038/s41570-018-0058-y.

[8] Xu C, Li X, Liu T, Zhang H. Design and synthesis of a free-standing carbon nano-fibrous web electrode with ultra large pores for high-performance vanadium flow batteries. RSC Adv 2017;7:45932–7. https://doi.org/10.1039/C7RA07365H.

[9] Liu Y, Zhou W, Lin Y, et al. Novel copper foam with ordered hole arrays as catalyst support for methanol steam reforming microreactor. Appl Energy 2019;246:24–37. https://doi.org/10.1016/j.apenergy.2019.03.199.

[10] Trogadas P, Ramani V, Strasser P, et al. Hierarchically Structured Nanomaterials for Electrochemical Energy Conversion. Angew Chem Int Ed 2016;55:122–48. https://doi.org/10.1002/anie.201506394.

[11] Charoen-amornkitt P, Alizadeh M, Suzuki T, Tsushima S. Entropy generation analysis during adjoint variable-based topology optimization of porous reaction-diffusion systems under various design dimensionalities. Int J Heat Mass Transf 2023;202:123725. https://doi.org/10.1016/j.ijheatmasstransfer.2022.123725.

[12] Charoen-amornkitt P, Alizadeh M, Suzuki T, Tsushima S. Topologically Optimized Anode Catalyst Layers of Proton Exchange Membrane Water Electrolyzers. ECS Trans 2023;111:87–95. https://doi.org/10.1149/11104.0087ecst.

[13] Alizadeh M, Charoen-amornkitt P, Suzuki T, Tsushima S. Mixed topology optimization: A self-guided boundary-independent approach for power sources. Energy Convers Manag 2023;294:117567. https://doi.org/10.1016/j.enconman.2023.117567.

[14] Tsushima S, Suzuki T. Modeling and Simulation of Vanadium Redox Flow Battery with Interdigitated Flow Field for Optimizing Electrode Architecture. J Electrochem Soc 2020;167:020553. https://doi.org/10.1149/1945-7111/ab6dd0.

[15] Donoso A, Aranda E, Ruiz D. A new method for designing piezo transducers with connected two-phase electrode. Comput Struct 2023;275:106936. https://doi.org/10.1016/j.compstruc.2022.106936.

[16] Kambampati S, Gray JS, Alicia Kim H. Level set topology optimization of structures under stress and temperature constraints. Comput Struct 2020;235:106265. https://doi.org/10.1016/j.compstruc.2020.106265.

[17] Roy T, Salazar De Troya MA, Worsley MA, Beck VA. Topology optimization for the design of porous electrodes. Struct Multidiscip Optim 2022;65:171. https://doi.org/10.1007/s00158-022-03249-2.

[18] Mitchell SL, Ortiz M. Computational multiobjective topology optimization of silicon anode structures for lithium-ion batteries. J Power Sources 2016;326:242–51. https://doi.org/10.1016/j.jpowsour.2016.06.136.

[19] Zheng X, Chen L, Luo J-W, et al. Topology optimization of diffusion–reaction processes in hierarchical porous structures. Chem Eng Sci 2024;287:119806. https://doi.org/10.1016/j.ces.2024.119806.

[20] Tomizawa M, Inoue G, Nagato K, et al. Heterogeneous pore-scale model analysis of micro-patterned PEMFC cathodes. J Power Sources 2023;556:232507. https://doi.org/10.1016/j.jpowsour.2022.232507.

[21] Zhang D, Forner-Cuenca A, Taiwo OO, et al. Understanding the role of the porous electrode microstructure in redox flow battery performance using an experimentally validated 3D pore-scale lattice Boltzmann model. J Power Sources 2020;447:227249. https://doi.org/10.1016/j.jpowsour.2019.227249.

[22] Kočí P, Isoz M, Plachá M, et al. 3D reconstruction and pore-scale modeling of coated catalytic filters for automotive exhaust gas aftertreatment. Catal Today 2019;320:165–74. https://doi.org/10.1016/j.cattod.2017.12.025.

[23] Chen L, Zhang R, Min T, et al. Pore-scale study of effects of macroscopic pores and their distributions on reactive transport in hierarchical porous media. Chem Eng J 2018;349:428–37. https://doi.org/10.1016/j.cej.2018.05.106.

[24] Zhang D, Cai Q, Taiwo OO, et al. The effect of wetting area in carbon paper electrode on the performance of vanadium redox flow batteries: A three-dimensional lattice Boltzmann study. Electrochim Acta 2018;283:1806–19. https://doi.org/10.1016/j.electacta.2018.07.027.

[25] Liu M, Shabaninejad M, Mostaghimi P. Impact of mineralogical heterogeneity on reactive transport modelling. Comput Geosci 2017;104:12–9. https://doi.org/10.1016/j.cageo.2017.03.020.

[26] Yang X, Mehmani Y, Perkins WA, et al. Intercomparison of 3D pore-scale flow and solute transport simulation methods. Adv Water Resour 2016;95:176–89. https://doi.org/10.1016/j.advwatres.2015.09.015.

[27] Wei X, Li W, Liu Q, et al. Pore-scale investigation on multiphase reactive transport for the conversion of levulinic acid to γ-valerolactone with Ru/C catalyst. Chem Eng J 2022;427:130917. https://doi.org/10.1016/j.cej.2021.130917.

[28] Sadeghi MA, Aghighi M, Barralet J, Gostick JT. Pore network modeling of reaction-diffusion in hierarchical porous particles: The effects of microstructure. Chem Eng J 2017;330:1002–11. https://doi.org/10.1016/j.cej.2017.07.139.

[29] van Gorp R, van der Heijden M, Sadeghi MA, et al. Bottom-up design of porous electrodes by combining a genetic algorithm and a pore network model. Chem Eng J 2023;455:139947. https://doi.org/10.1016/j.cej.2022.139947.

[30] Huang X, Zhou W, Liu B, Jiang K. Pore network modeling of advection-diffusion-reaction in porous media: The effects of channels. Chem Eng Sci 2023;271:118577. https://doi.org/10.1016/j.ces.2023.118577.

[31] Agnaou M, Sadeghi MA, Tranter TG, Gostick JT. Modeling transport of charged species in pore networks: Solution of the Nernst-Planck equations coupled with fluid flow and charge conservation equations. Comput Geosci 2020;140:104505. https://doi.org/10.1016/j.cageo.2020.104505.

[32] Qie Z, Rabbani A, Liang Y, et al. Multiscale investigation of pore network heterogeneity and permeability of fluid catalytic cracking (FCC) particles. Chem Eng J 2022;440:135843. https://doi.org/10.1016/j.cej.2022.135843.

[33] Gostick JT, Ioannidis MA, Fowler MW, Pritzker MD. Pore network modeling of fibrous gas diffusion layers for polymer electrolyte membrane fuel cells. J Power Sources 2007;173:277–90. https://doi.org/10.1016/j.jpowsour.2007.04.059.

[34] Sadeghi MA, Agnaou M, Barralet J, Gostick J. Dispersion modeling in pore networks: A comparison of common pore-scale models and alternative approaches. J Contam Hydrol 2020;228:103578. https://doi.org/10.1016/j.jconhyd.2019.103578.

[35] Hannaoui R, Horgue P, Larachi F, et al. Pore-network modeling of trickle bed reactors: Pressure drop analysis. Chem Eng J 2015;262:334–43. https://doi.org/10.1016/j.cej.2014.09.098.

[36] Moghaddam M, Abbassi A, Ghazanfarian J, Jalilian S. Investigation of microstructure effects on performance of hierarchically structured porous catalyst using a novel pore network model. Chem Eng J 2020;388:124261. https://doi.org/10.1016/j.cej.2020.124261.

[37] Gostick JT. Random Pore Network Modeling of Fibrous PEMFC Gas Diffusion Media Using Voronoi and Delaunay Tessellations. J Electrochem Soc 2013;160:F731–43. https://doi.org/10.1149/2.009308jes.

[38] Gostick J, Aghighi M, Hinebaugh J, et al. OpenPNM: A Pore Network Modeling Package. Comput Sci Eng 2016;18:60–74. https://doi.org/10.1109/MCSE.2016.49.

[39] Alizadeh M, Charoen-amornkitt P, Suzuki T, Tsushima S. A Numerical Simulation of Evolution Processes and Entropy Generation for Optimal Architecture of an Electrochemical Reaction-Diffusion System: Comparison of Two Optimization Strategies. J Electrochem Soc 2023;170:114520. https://doi.org/10.1149/1945-7111/ad0a7c.

[40] Alizadeh M, Charoen-amornkitt P, Suzuki T, Tsushima S. Investigation of transport-reaction dynamics and local/global entropy production in topology optimization of two-species reaction-diffusion systems. Chem Eng Sci 2023;275:118739. https://doi.org/10.1016/j.ces.2023.118739.

[41] Long M., Suzuki T., Alizadeh M., et al. The Influence of Rib and Porous Reactor Thickness on Topologically Optimized Structure in Reaction-Diffusion Systems. 2023 IEEE Transportation Electrification Conference and Expo, Asia-Pacific (ITEC Asia-Pacific). Chiang Mai, Thailand: IEEE; 2023. p. 1–7. doi:10.1109/ITECAsia-Pacific59272.2023.10372373.

[42] Lloyd S. Least squares quantization in PCM. IEEE Trans Inf Theory 1982;28:129–37. https://doi.org/10.1109/TIT.1982.1056489.

[43] Akbari M, Sinton D, Bahrami M. Viscous flow in variable cross-section microchannels of arbitrary shapes. Int J Heat Mass Transf 2011;54:3970–8. https://doi.org/10.1016/j.ijheatmasstransfer.2011.04.028.

[44] Bahrami M, Michael Yovanovich M, Richard Culham J. A novel solution for pressure drop in singly connected microchannels of arbitrary cross-section. Int J Heat Mass Transf 2007;50:2492–502. https://doi.org/10.1016/j.ijheatmasstransfer.2006.12.019.

[45] Wan S, Liang X, Jiang H, et al. A coupled machine learning and genetic algorithm approach to the design of porous electrodes for redox flow batteries. Appl Energy 2021;298:117177. https://doi.org/10.1016/j.apenergy.2021.117177.

[46] Papadopoulos S., Azar E. Optimizing HVAC operation in commercial buildings: A genetic algorithm multi-objective optimization framework. 2016 Winter Simulation Conference (WSC). Washington, DC, USA: IEEE; 2016. p. 1725–1735. doi:10.1109/WSC.2016.7822220.

[47] Yang M-D, Lin M-D, Lin Y-H, Tsai K-T. Multiobjective optimization design of green building envelope material using a non-dominated sorting genetic algorithm. Appl Therm Eng 2017;111:1255–64. https://doi.org/10.1016/j.applthermaleng.2016.01.015.

[48] Magnier L, Haghighat F. Multiobjective optimization of building design using TRNSYS simulations, genetic algorithm, and Artificial Neural Network. Build Environ 2010;45:739–46. https://doi.org/10.1016/j.buildenv.2009.08.016.

[49] Huang M, Ling Z, Sun C, et al. Two-stage damage identification for bridge bearings based on sailfish optimization and element relative modal strain energy. Struct Eng Mech 2023;86:715–30. https://doi.org/10.12989/SEM.2023.86.6.715.

[50] Huang M, Cheng X, Lei Y. Structural damage identification based on substructure method and improved whale optimization algorithm. J Civ Struct Health Monit 2021;11:351–80. https://doi.org/10.1007/s13349-020-00456-7.

[51] Deng Z, Huang M, Wan N, Zhang J. The Current Development of Structural Health Monitoring for Bridges: A Review. Buildings 2023;13:1360. https://doi.org/10.3390/buildings13061360.

[52] Gohardani SA, Bagherian M, Vaziri H, et al. A multi-objective imperialist competitive algorithm (MOICA) for finding motifs in DNA sequences. Math Biosci Eng 2019;16:1575–96. https://doi.org/10.3934/mbe.2019075.

[53] Li X, Xiao N, Claramunt C, Lin H. Initialization strategies to enhancing the performance of genetic algorithms for the p-median problem. Comput Ind Eng 2011;61:1024–34. https://doi.org/10.1016/j.cie.2011.06.015.

[54] Deb K, Agrawal S, Pratap A, Meyarivan T. A Fast Elitist Non-dominated Sorting Genetic Algorithm for Multi-objective Optimization: NSGA-II. In: Schoenauer M, Deb K, Rudolph G, editors. Parallel Problem Solving from Nature PPSN VI. Berlin Heidelberg, Berlin, Heidelberg: Springer; 2000. p. 849–58. https://doi.org/10.1007/3-540-45356-3_83.

[55] He Z, Gao M, Li Z, et al. Parametrized multi-objective seismic optimization for precast concrete frame with a novel post-tensioned energy dissipation beam-column joint. Comput Struct 2023;275:106911. https://doi.org/10.1016/j.compstruc.2022.106911.

[56] Fang Y, Li J. A Review of Tournament Selection in Genetic Programming. In: Liu Y, editor. Advances in Computation and Intelligence. Berlin Heidelberg, Berlin, Heidelberg: Springer; 2010. p. 181–92. https://doi.org/10.1007/978-3-642-16493-4_19.

[57] Blickle T, Thiele L. A Comparison of Selection Schemes Used in Evolutionary Algorithms. Evol Comput 1996;4:361–94. https://doi.org/10.1162/evco.1996.4.4.361.

[58] Fonseca C.M., Paquete L., Lopez-Ibanez M. An Improved Dimension-Sweep Algorithm for the Hypervolume Indicator. 2006 IEEE International Conference on Evolutionary Computation. Vancouver, BC, Canada: IEEE; 2006. p. 1157 – 1163. doi:10.1109/CEC.2006.1688440.